



# Quantifying stress distribution in ultra-large graphene drums through mode shape imaging



Ali Sarafraz<sup>1</sup>✉, Hanqing Liu<sup>1</sup>, Katarina Cvetanović<sup>2</sup>, Marko Spasenović<sup>2</sup>, Sten Vollebregt<sup>1</sup><sup>3</sup>, Tomás Manzaneque Garcia<sup>3</sup>, Peter G. Steeneken<sup>1,4</sup>, Farbod Alijani<sup>1</sup> & Gerard J. Verbiest<sup>1</sup>✉

Suspended drums made of 2D materials hold potential for sensing applications. However, the industrialization of these applications is hindered by significant device-to-device variations presumably caused by non-uniform stress distributions induced by the fabrication process. Here, we introduce a methodology to determine the stress distribution from their mechanical resonance frequencies and corresponding mode shapes as measured by a laser Doppler vibrometer (LDV). To avoid limitations posed by the optical resolution of the LDV, we leverage a manufacturing process to create ultra-large graphene drums with diameters of up to 1000 μm. We solve the inverse problem of a Föppl–von Kármán plate model by an iterative procedure to obtain the stress distribution within the drums from the experimental data. Our results show that the generally used uniform pre-tension assumption overestimates the pre-stress value, exceeding the averaged stress obtained by more than 47%. Moreover, it is found that the reconstructed stress distributions are bi-axial, which likely originates from the transfer process. The introduced methodology allows one to estimate the tension distribution in drum resonators from their mechanical response and thereby paves the way for linking the used fabrication processes to the resulting device performance.

The exceptional mechanical properties of suspended two-dimensional (2D) materials such as graphene make them ideal materials for applications such as force, mass, and sound sensing<sup>1–4</sup>. Their unique opto- and electro-mechanical coupling has enabled studies into phase transitions<sup>5</sup>, heat transport<sup>6,7</sup>, and even measuring the biological forces of micro-organisms<sup>8</sup>. However, the industrial realization of 2D materials is currently hindered by significant device-to-device variations observed in practice<sup>9</sup>. Addressing this variability is crucial for enhancing the reproducibility and reliability of 2D material-based devices. A key factor contributing to this variability is the built-in stress arising from the fabrication process<sup>9–11</sup>.

During the transfer of 2D materials onto target substrates, non-uniform stress distributions inevitably occur<sup>12,13</sup>, resulting in surface defects like wrinkles in the fabricated drums<sup>14–16</sup>. Currently, Raman spectroscopy and atomic force microscopy (AFM) are the methods of choice for analyzing the stress distribution in 2D materials<sup>17–19</sup>. Raman spectroscopy monitors the strain-sensitive position of Raman active phonon modes<sup>20</sup>. However, due to its limited spatial and strain resolution, it only provides a relatively

coarse strain measurement, making it less suitable for the quantification of the initial stress in suspended 2D materials. AFM is a contact-based technique that is challenging to perform and applies a force to the membrane during measurement. This force potentially affects the morphology and distribution of tension in the membrane. Consequently, the development of new non-contact methods that can determine the stress distribution in 2D membranes is highly desirable.

Determining the stress distribution in 2D materials has received limited attention within the literature. A common practice in the field is to assume a uniform stress distribution throughout the membrane<sup>21–25</sup>. This assumption is valid when the aspect ratio (thickness to radius ratio) of 2D material membranes increases, resulting in a bending rigidity-dominated mechanical response of the membrane. However, given that the primary advantage of 2D materials is in their high sensitivity for sensing applications, it is common that the aspect ratio is relatively small<sup>26</sup>, such that the membrane energy dominates the mechanical response<sup>27,28</sup>, which makes non-uniformities in the stress distribution significant<sup>29</sup>. This deviation can

<sup>1</sup>Department of Precision and Microsystems Engineering, Faculty of Mechanical Engineering, Delft University of Technology, Mekelweg 2, Delft, 2628 CD, The Netherlands. <sup>2</sup>Institute of Chemistry, Technology and Metallurgy, University of Belgrade, Njegoševa 12, Belgrade, 11000, Serbia. <sup>3</sup>Department of Microelectronics, Faculty of Electrical Engineering, Delft University of Technology, Mekelweg 4, Delft, 2628 CD, The Netherlands. <sup>4</sup>Kavli Institute of Nanoscience, Faculty of Applied Sciences, Delft University of Technology, Lorentzweg 1, Delft, 2628 CJ, The Netherlands. ✉e-mail: A.Sarafraz@tudelft.nl; G.Verbiest@tudelft.nl

significantly alter the mechanical behavior of the membranes, also leading to inaccuracies in estimating mechanical properties<sup>16,30-33</sup>. However, the modes of vibration of membranes are found to be very sensitive to spatial changes in the membrane<sup>29,34</sup>, thus providing the opportunity to use them for characterizing the non-uniform stress distribution.

In this paper, we propose a methodology to quantify the stress distribution of ultra-thin suspended drums by using nanomechanical resonances and their mode shapes. We use laser Doppler vibrometry (LDV)<sup>35</sup> to measure graphene drums, with large diameters from 60 to 1000  $\mu\text{m}$ , capturing their dynamics with picometer-amplitude resolution. Subsequently, we create an analytical model to calculate resonance frequencies and mode shapes. We then follow a reverse path by using experimental data to predict both in-plane and out-of-plane displacements, as well as the stress distribution of the 2D drum. Our results highlight that 2D material drums are not uniformly tensioned, which challenges the current methodologies for estimating the built-in stress of these drums<sup>19,20</sup>. The presented methodology allows fabrication techniques to be optimized for improving the uniformity and reproducibility of stress distributions, thus improving the yield and performance of sensing applications based on suspended 2D material membranes.

## Results

### Experimental signs of non-uniform stress distribution

We created 16 suspended graphene devices and measured their resonance response (see Methods). To extract their resonances, we employ a fitting procedure based on a linear harmonic oscillator model. The frequency characteristics of the first mode ( $f_1 = \frac{\omega_1}{2\pi}$ ) in devices D1–D16, as a function of the radius  $R$ , are depicted in Fig. 1a. The observed dependence on  $R$  aligns with the behavior reported earlier on the fundamental frequencies of circular drums<sup>36</sup>. The relationship governing the resonance frequencies is described by the equation

$$f_i = \frac{\gamma_i}{2\pi R} \sqrt{\frac{n_0}{\rho h}} \quad (1)$$

where  $\gamma_i$  represents a constant,  $n_0$  denotes the pre-tension applied to the drum,  $\rho$  signifies the mass density, and  $h$  stands for the thickness of the drum. Theory gives  $\gamma_1 = 2.4048$ , with higher resonance frequencies corresponding to increased values of  $\gamma_i$  relative to  $\gamma_1$ . Since  $R$  and  $h$  are known for our samples from optical microscopy and AFM measurements, we can extract  $n_0$  of the devices using the first resonance frequency  $f_1$  by utilizing Eq. (1). We note that the obtained  $n_0$  varies from  $2 \times 10^{-3}$  to  $3 \times 10^{-1} \text{ N m}^{-1}$ , which is comparable to the range of values reported in the literature<sup>37,38</sup>. The corresponding strain  $\epsilon_0$  extracted from  $n_0 = \sigma_0 h = Eh\epsilon_0/(1 - \nu)$  is below 0.0013% for all our devices, which is much lower than the resolution limits of Raman spectroscopy<sup>39</sup>.

In Fig. 1b, we plot the ratio between the second and the first resonance frequency of 16 fabricated devices. We also show in Fig. 1b the  $f_2/f_1$  obtained analytically for circular drums (red line). We note that the experimental values of  $f_2/f_1$  significantly deviate from this red line with a minimum ratio of 1.019 and a maximum ratio of 1.754. To gain insight into these deviations, in Fig. 1c, we show the experimental mode shapes, as determined by the MSA-400 vibrometer, for three of the devices. We note clear differences between the second theoretical mode shape of a circular drum and the experimental mode shape, which emphasizes the substantial influence of non-uniform stress on the dynamics of these drums. In addition, we analyze the ratios  $f_3/f_1$  and  $f_4/f_1$  for a specific subset of our drums (see Supplementary Note 1), in which we also observe a significant difference between the experimental findings and the theoretical predictions based on the assumption of uniform pre-tension.

In addition, it has been theoretically predicted that when a stress distribution is uniform, it results in the emergence of asymmetric mode shapes that are defined by  $n$  nodal lines rotated by  $2\pi/n$  relative to each other and possess equal resonance frequencies<sup>27</sup>. Nevertheless, as the level of stress non-uniformity increases, these mode shapes undergo substantial changes resulting in a loss of resemblance between them. Consequently, the non-uniformity in tension distribution has a substantial effect on the mode-shapes, and therefore these mode-shapes contain important information on the stress distribution. In the subsequent section, we introduce a method to deduce the non-uniform tension distribution based on the experimentally acquired mode shapes and resonance frequencies.

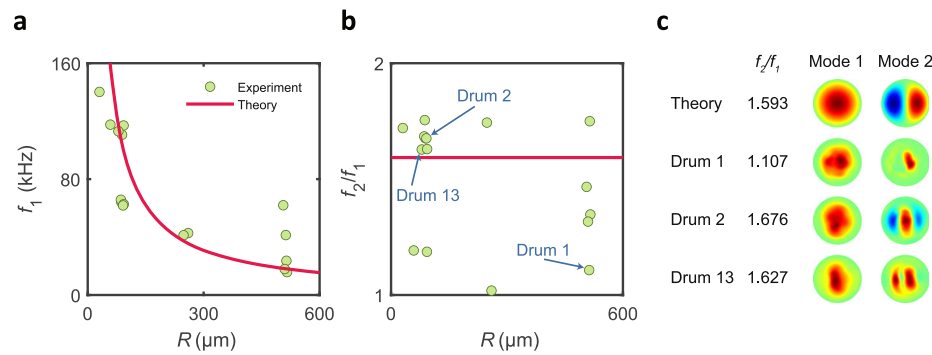
### Theory for quantifying stress distribution

To analyze the effect of stress distributions on the mode-shapes of the drums, we employ a circular plate model characterized by radius  $R$  and thickness  $h$ . This model assumes the material to be homogeneous and isotropic, having a density  $\rho$ , Young's modulus  $E$ , and Poisson's ratio  $\nu$ . It is worth noting that plate and membrane models have demonstrated accuracy in predicting the mechanical behavior of 2D material membranes<sup>31,40</sup>. To date, there is no evidence indicating their inapplicability to single- or few-layer 2D materials. Moreover, we assume the structure to be relatively thin, i.e.,  $h/R \leq 0.1$ <sup>27</sup>, such that we can utilize the Föppl–von Kármán plate model. Employing this model enables us to capture the dynamics of drums with a wide range of thickness-to-radius ratios (aspect ratio). The governing equations are expressed in cylindrical coordinates  $(r, \theta, z)$ , with  $r$  representing the radial,  $\theta$  the azimuthal, and  $z$  the transverse coordinate. The equations governing transverse and in-plane motions, derived through Hamilton's principle, are given by:

$$\rho h \ddot{w} + D \nabla^4 w - (N w) = 0, \quad (2a)$$

$$\rho h \ddot{u} - N = 0, \quad (2b)$$

**Fig. 1 | Comparison of experimental results with uniform pre-tension.** **a** The relationship between the fundamental frequency  $f_1$  and the drum radius  $R$  for devices D1–D16 is observed to exhibit an inverse trend. Resonance frequency estimation using Eq. (1) is shown in red, by assuming thickness  $h = 15 \text{ nm}$  and pre-tension  $n_0 = 0.02 \text{ N m}^{-1}$ . **b** The ratio of the second to the first frequency ( $f_2/f_1$ ) as a function of  $R$  for all studied devices. The theoretical value of  $f_2/f_1$  for drums having uniform pre-tension is shown by the red line. **c** The first and second mode shapes and the corresponding frequency ratio of three of the measured devices and their comparison to theoretical estimates based on Eq. (1). All mode shapes are normalized with respect to the maximum value of their displacement and the colorbar ranges between  $-1$  and  $1$ .



where

$$\begin{aligned} N &= [Eh/(1-\nu^2)][(1-\nu)\epsilon + \nu \operatorname{tr}(\epsilon)I], \\ \epsilon &= \frac{1}{2}(\nabla \mathbf{u} + \nabla^T \mathbf{u} + \nabla w \otimes \nabla w). \end{aligned} \quad (3)$$

In the equations above,  $\mathbf{u} = [u; v]$ , with  $u$  and  $v$  denoting the radial and azimuthal displacement fields, while  $w$  represents the transverse displacement field. Additionally,  $\nabla^4 w$ ,  $\nabla w$ , and  $\nabla \mathbf{u}$  denote the biharmonic operator applied to the scalar field  $w$ , the vector gradient of the scalar field  $w$ , and the tensor gradient of the vector field  $\mathbf{u}$ , respectively.  $N$  is vector divergence of the tensor field  $N$ . Furthermore,  $\nabla w \otimes \nabla w$  corresponds to the tensor product between vectors  $\nabla w$  and  $\nabla w$ . An overdot indicates differentiation with respect to time, and  $D = \frac{Eh^3}{12(1-\nu^2)}$  denotes the bending rigidity. It is noteworthy that, as per the notation presented here, the strain tensor  $\epsilon$  and stress resultant tensor  $N$  can be identified as second-order tensors in a two-dimensional framework.

In practice, fabricated drums may exhibit deformations that deviate from the conventional assumption of uniform radial deformation, often associated with uniform pre-tension. Consequently, when these drums undergo transverse dynamic actuation, their displacement fields comprise both static and dynamic components. The static deformation originates from the pre-actuation displacement history, while the dynamic component represents the displacement induced by the actuation process. To gain a comprehensive understanding of the mechanical response in such situations, it becomes essential to incorporate both static and dynamic displacements within the overall displacement field<sup>41–43</sup>. However, the substantial difference in magnitude between in-plane and transverse inertia (proportional to  $R/h$ ) necessitates the exclusion of dynamic deformation in the in-plane direction. This is due to the fact that, based on Newton's second law, higher inertia leads to lower acceleration and dynamical response. Thus, in-plane motion is negligible compared to the out-of-plane dynamics when studying bending vibrations of thin membranes. Therefore, we assume  $\mathbf{u} = \mathbf{u}_s$ , but  $w = w_s + w_d$ , where the subscript  $s$  refers to static components and the subscript  $d$  represents dynamic deformations.

To capture the vibrational response ( $w_d$ ) of these drums, we conduct a modal analysis using Eq. (2a) centered around the statically deformed configuration  $(u_s, v_s, w_s)$ . However, since Eq. (2a) involves  $N$  and is not expressed in terms of displacement fields, we initially reformulate the equation in the context of static and dynamic displacement fields. The detailed derivation procedure for this can be found in Supplementary Note 2. Next, we assume the dynamic transverse deformation  $w_d$  to be harmonic and express it as  $w_d(r, \theta, t) = w_d^0 \varphi(r, \theta) \exp(i\omega t)$ , where  $w_d^0$  represents the maximum spatial amplitude of the drum at time  $t = 0$ ,  $\varphi(r, \theta)$  denotes the mode shape normalized with respect to maximum displacement, and  $\omega$  is the corresponding resonance frequency. Next, we make the equations dimensionless (see Supplementary Note 2) and discretize them over a mesh with  $N$  nodes in the radial direction and  $M$  nodes ( $M$  should be odd) in the azimuthal direction (see Supplementary Note 3), which leads to the compact form of the transverse governing equation

$$\mathbf{D}_U U_{ij} + \mathbf{D}_V V_{ij} + \sum_k (\bar{\mathbf{D}}_W^k W_{ij}) \cdot (\bar{\mathbf{D}}_W^k W_{ij}) = (\bar{\omega}^2 I - \mathbf{D}_W) \Phi_{ij}, \quad (4)$$

where  $U_{ij}$ ,  $V_{ij}$ , and  $W_{ij}$  represent the unknown static deformations at spatial node  $(i, j)$ . Additionally,  $\Phi_{ij}$  is the given (or known) normalized mode shape extracted from the experiments,  $\bar{\omega}$  denotes the corresponding non-dimensional resonance frequency, and  $I$  is the identity matrix. Moreover, the matrices  $\mathbf{D}_U$ ,  $\mathbf{D}_V$ ,  $\mathbf{D}_W$ ,  $\bar{\mathbf{D}}_W^k$ , and  $\bar{\mathbf{D}}_W^k$  denote linear differential operators dependent on the mode shapes and discretization weighting coefficients. Comprehensive details regarding this step can be found in Supplementary Note 3. After a convergence study, we choose  $N = 161$  and  $M = 91$  to ensure a good balance between computational speed and accuracy of the results. It should be mentioned that this selection may change for drums with different aspect ratios.

Unlike the conventional modal analysis, where predefined static deformations  $U_{ij}$ ,  $V_{ij}$ , and  $W_{ij}$  are used to deduce resonance frequencies  $\bar{\omega}$  and mode shapes  $\Phi_{ij}$  in our approach, we follow a reverse-path, and deduce these deformations from measured resonance frequencies and mode shapes. Given the existence of three unknown displacement fields, specifically  $U_{ij}$ ,  $V_{ij}$ , and  $W_{ij}$  ( $3 \times M \times N$  unknowns), the extraction of these displacement fields necessitates a minimum of  $3 \times M \times N$  equations. This underscores the significance of having no fewer than three sets of mode shapes ( $\Phi_{ij}^1, \Phi_{ij}^2, \Phi_{ij}^3$ ), along with their corresponding non-dimensional frequencies ( $\bar{\omega}_1, \bar{\omega}_2, \bar{\omega}_3$ ) for estimating the built-in stress, which collectively provides  $3 \times M \times N$  equations across the mesh (see Eq. (4)). However, in practice, an additional mode shape becomes a crucial requirement. The underlying rationale for this is rooted in the observation that equations linked to boundary nodes yield a trivial  $0 = 0$  relationship. Consequently, introducing supplementary equations is necessary to fulfill the requisite rank of the algebraic equation system. In pursuit of accurately determining stress distributions from experimental mode shapes and frequencies, it thus becomes essential to consider at least four mode shapes alongside their corresponding resonance frequencies.

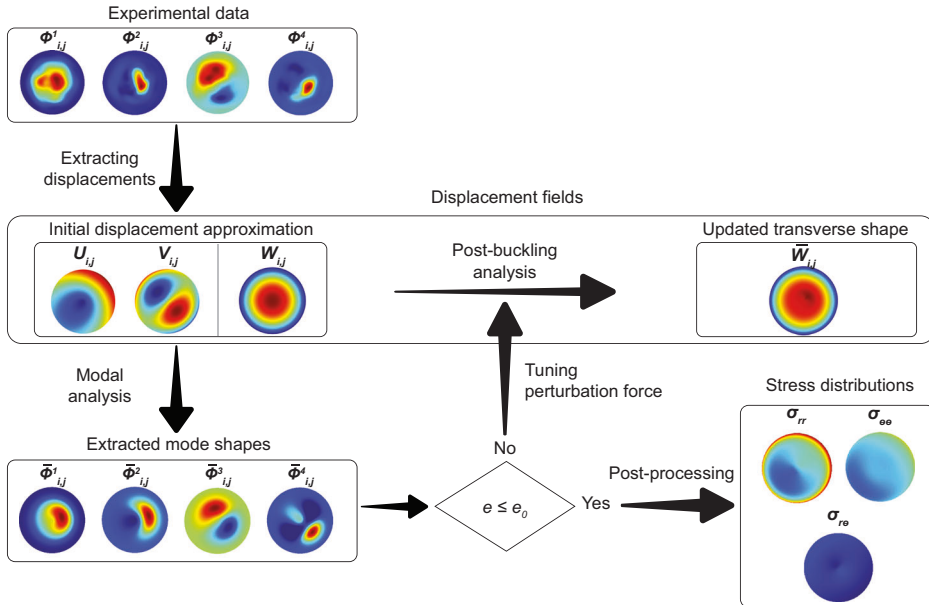
To validate our numerical methodology and equations, we performed finite element simulations on a flat circular plate characterized by a pre-defined non-uniform stress distribution. The computed mode shapes and resonance frequencies were then employed to reconstruct the stress distribution using the methodology we have introduced (for detailed discussion, see Supplementary Note 4).

By simultaneously using the governing Eq. (4) for a minimum of four mode shapes and the respective resonance frequencies, it becomes possible to determine the static displacement fields and the associated stress distribution fields. The flowchart presented in Fig. 2 explains the sequential approach for obtaining stress distributions from experimental mode shapes and frequencies. The technique commences by fitting a surface to the experimental mode shapes. This is important as Eq. (4) involves derivative operators, and any non-smoothness and noise in experimental mode shapes leads to numerical inaccuracies<sup>30</sup>. In order to guarantee compliance with boundary conditions, we utilize the mode shapes of a uniformly-tensioned plate as the basis for our fitting function (see Supplementary Note 5).

Subsequently, utilizing the smoothed mode shapes, we aim to extract the static displacement fields. However, due to the nonlinearity of Eq. (4) with respect to  $W_{ij}$ , extracting the solution without a suitable initial approximation poses a challenge. As a possible solution, we assume a parabolic form for the static transverse displacement, characterized by an undetermined deflection amplitude at the center of the drum ( $W_{ij} = W_0(1 - \bar{R}_{ij}^2)$ ), where  $W_0$  signifies the deflection at the center, and  $\bar{R}_{ij}$  represents the  $r$ -coordinate of node  $(i, j)$ . By solving Eq. (4) using the experimentally acquired mode shapes  $\Phi_{ij}^1, \Phi_{ij}^2, \Phi_{ij}^3$ , and  $\Phi_{ij}^4$ , we can determine the unknowns  $U_{ij}$ ,  $V_{ij}$ , and  $W_0$ . It is crucial to recognize that due to the influence of noise and measurement inaccuracies, achieving 100% accuracy in solving for displacements is unattainable. Therefore, employing a least-squares method becomes necessary. This method enhances accuracy by incorporating more equations, namely additional mode shapes and frequencies, into the solution process.

It is imperative to acknowledge that assuming an axisymmetric parabolic deflection for the transverse displacement has inherent limitations. The presence of non-uniform displacements in the studied membranes might lead to static deformation and the creation of a buckling pattern, owing to their ultra-thin nature. Due to experimental and numerical inaccuracies, the displacement fields that are obtained from solving Eq. (4) do not always meet the requirements of the in-plane Eq. (2b). Therefore, it is crucial to identify a stable out-of-plane configuration that fulfills Eq. (2a). In response to potential static transverse asymmetries and to rectify our initial assumption of parabolic static deformation, we perform a post-buckling analysis. This analysis utilizes the in-plane displacement fields  $U_{ij}$ ,  $V_{ij}$ , and  $W_{ij}$ , which are obtained from the experimental mode shapes to update transverse displacement  $W_{ij}$  to  $\bar{W}_{ij}$ . In the context of this post-buckling analysis, a minor perturbing uniform transverse force is introduced, which

**Fig. 2 | The flowchart for deriving stress distributions from experimental mode shapes and resonance frequencies.** Assuming a parabolic deformation in the transverse direction, the experimental mode shapes are first employed to extract initial displacement fields. Then a modal analysis is performed. If the extracted mode shapes do not match the experimental ones sufficiently ( $e > e_0$ ), the perturbation force is tuned, and using a post-buckling analysis, the transverse shape is modified. After that, using in-plane displacement fields and the updated transverse displacement, we again obtain theoretical mode shapes and resonance frequencies. If the mode shapes do not satisfy the criterion (5), we recalculate the transverse shape by adjusting the perturbation force to the post-buckling step. From there, we return to the modal analysis. When the convergence criterion is met, the obtained displacement fields are used to calculate stress distributions. Here,  $i = 1, 2, \dots, N$ , and  $j = 1, 2, \dots, M$  denotes the node number in radial, and azimuthal directions. Here, colorbars for  $\Phi_{i,j}^1, \Phi_{i,j}^2, \Phi_{i,j}^3, \Phi_{i,j}^4, \bar{\Phi}_{i,j}^1, \bar{\Phi}_{i,j}^2$ , and  $\bar{\Phi}_{i,j}^4$  range from 0 to 1, while those for  $\Phi_{i,j}^3$  and  $\bar{\Phi}_{i,j}^3$  range from -1 to 1. The colorbar for  $U_{i,j}$  spans 0.25–1.75 nm, for  $V_{i,j}$  from -0.2 to 0.2 nm, and for  $W_{i,j}$  and  $\bar{W}_{i,j}$  from 0 to 300 nm. Additionally,  $\sigma_{rr}, \sigma_{r\theta}$ , and  $\sigma_{\theta\theta}$  range from 0 to 10 MPa.



serves to update the drum's transverse shape and accounts for its nonlinear behavior<sup>44</sup>.

In order to perform the post-buckling analysis, it is recommended to utilize Eqs. (2a, b) or alternatively, incorporate the in-plane displacement fields ( $U_{i,j}$  and  $V_{i,j}$ ) into a finite element method (FEM) software that is capable of handling nonlinear structural analysis. This will enable an analysis of the post-buckling response of the drum and the establishment of its modified transverse shape  $\bar{W}_{i,j}$ . It is crucial to highlight that as a result of the non-uniform characteristics of  $U_{i,j}$  and  $V_{i,j}$ , the post-buckling analysis results in an asymmetric transverse shape  $\bar{W}_{i,j}$  that deviates from the axisymmetric shape  $W_{i,j}$ .

Since, the experimental displacement field is not known for the drums and in order to ensure accurate computation of both in-plane and transverse displacement fields, we conduct modal analysis to extract mode shapes and resonance frequencies from the static displacements ( $U_{i,j}, V_{i,j}$ , and  $\bar{W}_{i,j}$ ). It should be noted that Eq. (4) shows a one-to-one mapping between mode shapes and displacement fields, thus the comparison between the mode shapes can directly reflect the comparison between the static displacement fields. In order to quantitatively assess the fidelity of the reconstructed mode shapes compared to their experimental counterparts, we employ an error metric denoted by  $e$ . This metric  $e$  characterizes the average spatial deviation between the reconstructed and experimental mode shapes and is defined as follows

$$e = \frac{1}{\bar{N}} \sum_{n=1}^{\bar{N}} \left[ \frac{\int_0^{2\pi} \int_0^1 (\bar{\varphi}_n - \varphi_n)^2 r dr d\theta}{\int_0^{2\pi} \int_0^1 (\varphi_n)^2 r dr d\theta} \right]^{1/2} \leq e_0, \quad (5)$$

where  $e_0$  serves as an error threshold. In this equation,  $\bar{\varphi}_n$  is the  $n$ th normalized mode shape obtained from modal analysis,  $\varphi_n$  signifies the  $n$ th normalized experimental mode shape, and  $\bar{N}$  represents the total number of mode shapes used in the fitting procedure. It is important to note that both  $\bar{\varphi}_n$  and  $\varphi_n$  are the continuous forms of  $\Phi_{i,j}^n$  and  $\bar{\Phi}_{i,j}^n$ , respectively.

If the criterion (5) is satisfied ( $e \leq e_0$ ), the solution is considered to be converged. Conversely, if  $e > e_0$ , the post-buckled configuration is recalculated with a new perturbation in the transverse direction, leading to the

acquisition of an updated transverse mode shape. This iterative process continues until the convergence criterion is met.

To determine an appropriate value for  $e_0$ , we initiate the iterative process without applying any perturbation force and gradually increase it step-by-step. The observed trend reveals an initial decrease in the error metric  $e$  as the perturbation force rises until it reaches the minimum value  $e_0$  at a perturbation force of  $\delta p_m$ . Beyond this point, further increments in the perturbation force result in an increase in the error. Consequently, the minimum achievable error for each set of experiments corresponds to  $e_0$ , which varies among different drums. For instance, device D1 exhibits an error threshold of  $e_0 \simeq 0.19$ . A more detailed and comprehensive discussion regarding the determination of  $e_0$  can be found in Supplementary Note 6.

Once the solution has converged, the numerical displacement field effectively approximates the experimental displacement field, which enables us to compute the strain field and subsequently derive the stresses within the drum's mid-plane using Supplementary Eqs. (2) and (3). For a more comprehensive overview of the described procedure, including a detailed flowchart, please consult the Supplementary Note 5.

### Fitting procedure

As elaborated in the previous section, the numerical procedure necessitates an initial assumption of a parabolic transverse displacement field. However, this assumption does not universally apply to all manufactured devices. Some of the manufactured devices exhibit significant complex wrinkling patterns that deviate noticeably from the parabolic approximation. Consequently, the proposed method is not applicable to drums that deviate from this assumption.

Among the devices produced for this study, four of them (D1, D2, D6, and D13) exhibited minimal or negligible wrinkling patterns, making them well-suited candidates for the proposed solution outlined in this study. For these four drums, we quantified stress distributions and validated their accuracy by reconstructing mode shapes using the derived stresses. In Fig. 3, we provide an illustrative example showcasing both the experimental mode shapes and the reconstructed mode shapes for device D1, utilizing the first four distinct mode shapes. It is evident that the obtained stress distribution was able to accurately reconstruct the experimental mode shapes with a high

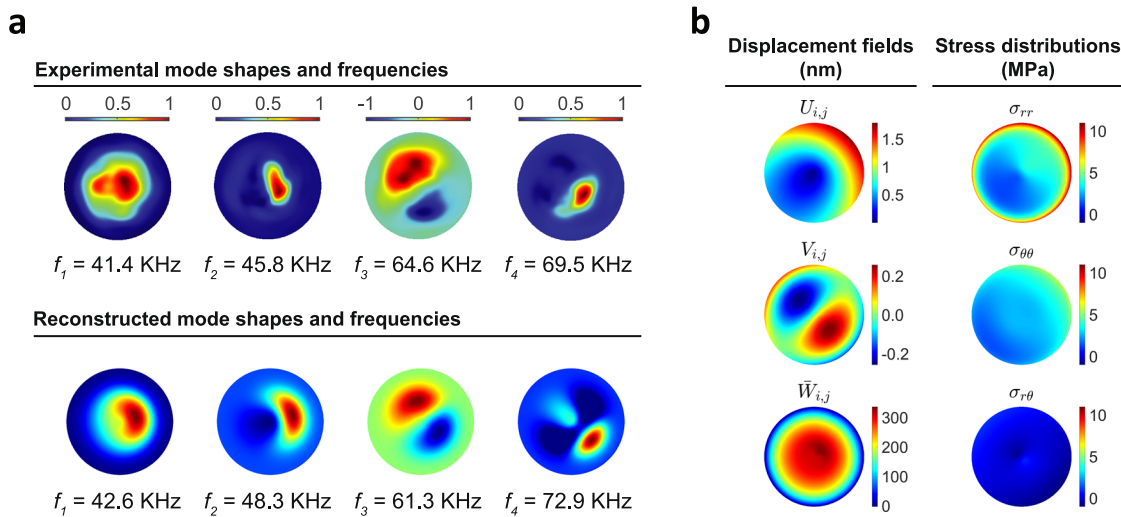


**Fig. 3 | Reconstruction of stress distributions based on experimental mode shapes for device D1.** **a**, Comparison of experimental mode shapes and resonance frequencies and reconstructed counterparts. As described in the main text, the experimental mode shape and frequencies are utilized to derive displacement fields and stress distributions. For the purpose of determining the validity of the results, the

theoretical mode shapes are reconstructed using the displacement field.

**b**, Displacement fields and Stress distributions predicted by current method. As can be seen assumption of uniform stress distribution is not valid for the manufactured device.

level of accuracy. The results for devices D2, D6, and D13 are presented in Supplementary Note 7.

Moreover, to highlight the fidelity of the proposed method, we present the extracted displacement field and the corresponding non-uniform stress distributions in Fig. 3. Note that Raman spectroscopy, which we utilized for stress measurement, is limited in its ability to detect the non-uniformity of stress within the drum (see Supplementary Note 8). The predicted stress distribution obtained through Raman spectroscopy appears to be nearly constant and uniform, with large uncertainty across the drum surface. This is due to the fact that the strain values ( $\epsilon < 0.0013\%$ ) are lower than the resolution limit (0.1%) of Raman spectroscopy<sup>20,39,45</sup> (see Methods). In the Supplementary Note 8, a thorough discussion of the Raman spectroscopy measurements and the obtained stress distributions for device D1 is provided. In contrast, the presented methodology is founded upon continuum mechanics which is not dimension-dependent. As a result, the resolution of this method is primarily constrained by the measurement device's capability to discern mode shapes. Consequently, the method's efficacy remains unaffected by the size of the drum or the scale of its strain distributions. This implies that even for small drums with radii on the order of a few micrometers, our methodology can measure strain and stress distributions, regardless of the magnitude of the strains. Hence, this approach remains applicable across a range of scales, encompassing relatively small drums.

To compare the extracted stress distributions and the nominal stress values obtained assuming a uniform tension distribution, we calculated the spatial averages of normal and shear stresses by

$$\bar{\sigma}_{ij} = \frac{\int_0^{2\pi} \int_0^R \sigma_{ij} r dr d\theta}{\pi R^2}, \quad (6)$$

where  $i, j = \{r, \theta\}$ . To measure the robustness of our findings, we systematically adjusted the level of mode shape fitting during the preliminary stage (see Supplementary Eq. (3)). This variation allowed us to quantitatively determine the associated standard deviation and obtain valuable insights into the sensitivity of our stress distribution analysis. To determine the nominal stress  $\sigma_0$  under the assumption of a uniform tension distribution, we employed the first resonance frequencies, considering them as resonances of an ideal theoretical drum subjected to uniform tension (see Eq. (1)). Notably, the spatial average of shear stress for all four drums was found to be negligible. However, this was not the case for the values of  $\bar{\sigma}_{rr}$  and  $\bar{\sigma}_{\theta\theta}$ , which demonstrated appreciable differences. The computed average stress

values, obtained through our analysis and assuming uniform stress distribution, are both presented in Table 1.

The differences observed between the average values of  $\bar{\sigma}_{rr}$  and  $\bar{\sigma}_{\theta\theta}$  in Table 1 contradict the uniform stress assumption, which posits that  $\bar{\sigma}_{rr} = \bar{\sigma}_{\theta\theta} = \sigma_0$ . Notably, a greater deviation of  $\bar{\sigma}_{rr}$  from  $\bar{\sigma}_{\theta\theta}$  indicates a higher degree of non-uniformity in the stress distribution within the drum. The observed differences between the average values of  $\bar{\sigma}_{rr}$  and  $\bar{\sigma}_{\theta\theta}$  raise doubts about the validity of the uniform stress assumption. Specifically,  $\sigma_0$  is at least 47% greater than the mean value of  $\bar{\sigma}_{rr}$  for each of the drums. This finding suggests that spatially averaging the stress distributions will not yield a uniform stress representation of the overall behavior of the studied drums. Therefore, accounting for the non-uniformities is essential for proper estimation of the built-in stress in ultra-thin membranes.

Our method's effectiveness is further evident in Fig. 3, where we observe the influence of a free edge on the displacement and stresses of the drum. The microscope image of device D1, as depicted in Fig. 4d, clearly demonstrates that one side of the drum is clamped, while the other side remains unclamped and capable of free movement. Surprisingly, this free edge has influenced the results by exhibiting less radial displacement and, consequently, lower stresses on the free side. This finding supports the intuition that a free edge allows the drum to mechanically release stresses near the edge.

## Discussion

The proposed methodology addresses a system of nonlinear equations (Eq. (4)), under the assumption of a parabolic transverse static displacement field. However, when the drum exhibits initial corrugations or wrinkles that cannot be adequately characterized by such a parabolic

**Table 1 | Spatial average value of non-uniform stress distribution in comparison with nominal stress value assuming uniform stress distribution in the drums**

Device	$\bar{\sigma}_{rr}$ (MPa)	$\bar{\sigma}_{\theta\theta}$ (MPa)	$\sigma_0$ (MPa)
D1	$3.76 \pm 0.25$	$2.80 \pm 0.29$	7.05
D2	$0.65 \pm 0.06$	$0.53 \pm 0.08$	1.36
D6	$0.54 \pm 0.09$	$0.33 \pm 0.07$	0.94
D13	$1.03 \pm 0.21$	$0.49 \pm 0.10$	1.52

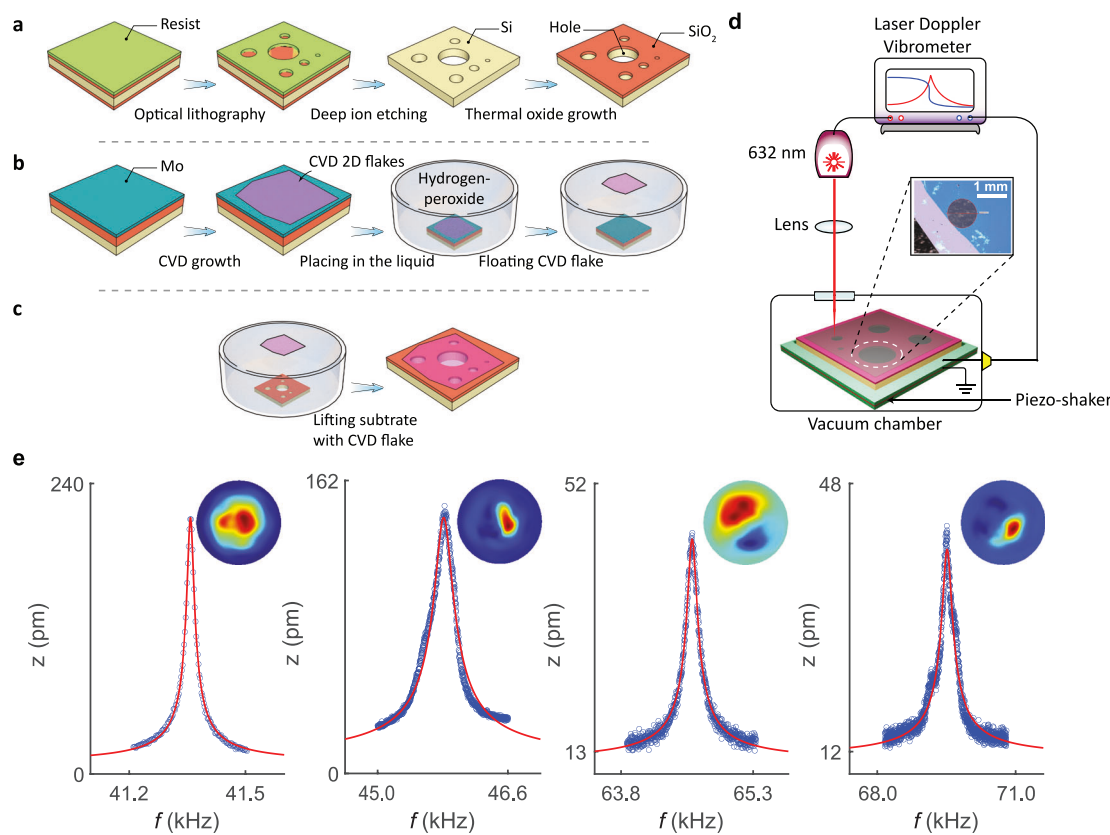


**Fig. 4 | Fabrication and vibration measurement of graphene drums.** **a** Fabrication process of  $\text{SiO}_2/\text{Si}$  substrate with etched holes. **b** Growth and exfoliation of large-scale CVD graphene flake. **c** Wet transfer method to suspend CVD graphene on the substrate. **d** Schematic of measurement setup comprising an MSA400 polytec laser doppler vibrometer (LDV) for detection and read-out. The sample is placed in the vacuum chamber and driven by a piezo shaker. The inset: optical image of device D1;

purple region,  $\text{Si}/\text{SiO}_2$  substrate; blue region, supported graphene; transparent region, suspended graphene. **e** The first four resonances of device D1; the damped linear harmonic oscillator fit is shown by the red line. Here, colorbars for first, second, and fourth mode shapes range from 0 to 1, while that for third ranges from  $-1$  to 1.

displacement field, the system of equations becomes challenging to solve. In such scenarios, the equations need to be solved by providing a suitable initial guess for the transverse displacement field  $W_{i,j}$ . To estimate the static transverse displacement field of the drum in the presence of these non-parabolic deformations, corrugations should be experimentally probed. Several techniques are available for measuring these out-of-plane deformations<sup>46,47</sup> and can aid with quantifying the tension distribution.

Notably, microscopic images of the drums (see Supplementary Fig. 1) do not always reveal signs of transverse bulges or wrinkles, despite their presence. Although the transverse displacement is relatively small compared to the drum's radius ( $W_0/R \leq 0.001$ ), neglecting it in the modal analysis can lead to inaccurate mode shape estimations and, ultimately, even to failure in reconstructing the experimental mode shapes. Moreover, even minor static transverse asymmetries can affect the expected mode shapes<sup>44,48</sup>, emphasizing the need for an accurate solution to capture these deviations. This emphasizes the importance of the transverse displacement field when reconstructing the stress distribution.

Owing to inherent experimental uncertainties and noise, there exists a lower bound on the threshold  $e_0$ . For device D1, the estimated experimental noise on each mode shape is 3%, 4%, 18%, and 20%, respectively, leading to a lower average bound for  $e_0$  of 11%. To enhance the precision of measuring  $e_0$ , employing measurement devices with higher spatial resolution and lower noise levels is recommended.

The comprehensive study of drums yielded valuable insights into their stress distributions. These drums experience uniaxial or biaxial loading with different loadings along the two axes, suggesting non-uniform biaxial tension induced in the manufacturing process. This understanding is crucial for

optimizing manufacturing processes to achieve uniform stress distribution and flatness in the drums.

The proposed method is specifically tailored for thin drums, taking into account both stretching and bending energies to derive the governing equations and ensure numerical stability. As a result, two distinct mechanisms govern the mode shapes and resonance frequencies. In cases where stretching dominates the deformation of the drum, the pre-stresses play a significant role in influencing its vibrational behavior. This scenario is particularly relevant for drums with a height-to-radius ratio  $h/R \leq 0.001$ . Conversely, as bending deformation becomes more prevalent in over-stretching, the vibrational behavior of the drum is primarily governed by bending energies, with pre-stresses having a marginal role. In such instances, the accuracy of the proposed method may be compromised, as the mode shapes are predominantly influenced by bending effects rather than stress distributions. However, it is important to mention that when the aspect ratio is large, the mechanics of the drums are mostly influenced by the bending mechanism, while the effect of stress distribution becomes insignificant. Nevertheless, the maximum ratio of thickness to radius ( $h/R$ ) observed in the drums manufactured in our study is roughly 0.00023 (see Supplementary Table 1), which confirms that the drums analyzed in our work are membranes with negligible bending rigidity. Therefore, the established model proves suitable for addressing the problem.

Despite this limitation, in practical applications, the first scenario ( $h/R \leq 0.001$ ) is often encountered, rendering the proposed method suitable and reliable for analyzing the vibrational behavior of drums. It is worth noting that as  $h/R$  increases, the bending deformations become more energy-costly, resulting in drums with fewer corrugations and wrinkles. Unfortunately, this also leads to reduced sensitivity to transverse loadings

and masses. Hence, the choice of  $h/R$  becomes critical in designing circular drums to achieve the desired vibrational characteristics and performance for specific applications.

It is important to ensure that the method proposed is applicable to thinner devices or membranes of smaller dimensions. Here, we should highlight that our approach is based on continuum mechanics and thus size-independent. Yet, to affirm the applicability of our method to thinner and smaller graphene membranes, we utilized the experimental data of<sup>34</sup> for a graphene drum ( $h = 10$  nm,  $d = 5$   $\mu$ m), and reconstructed the non-uniform tension successfully (see Supplementary Note 9).

It is also noteworthy that the methodology proposed herein is not limited solely to graphene membranes but is applicable to a broader range of thin films and 2D material membranes. In our analysis, we adopted a linear isotropic material model to predict material behavior. However, if other 2D material membranes exhibit discrepancies in material behavior, such as anisotropy<sup>49</sup>, these can be incorporated into the proposed method through constitutive law (Supplementary Eq. (3)). This allows for the extension of the formulation to accommodate studying of various types of 2D material membranes.

In conclusion, we presented a methodology for quantitative determination of the tension distribution in ultra-thin 2D material drums based on experimental mode shapes and resonance frequencies. By utilizing a circular plate model, we derived governing equations that capture the static and dynamic deformation of the drums. The proposed approach successfully accounts for both stretching and bending energies, providing an effective solution for analyzing the vibrational behavior of circular drums.

The validation of the method through finite element simulations on known stress distributions demonstrates its accuracy and reliability. We applied the methodology to four fabricated drums and gained valuable insights into their stress distributions. The findings revealed the presence of non-uniform biaxial tension induced during the manufacturing process. Understanding these stress distributions is critical for optimizing the fabrication processes to achieve uniform stress distribution and flatness in the drums.

Additionally, we discussed the limitations related to the assumption of a parabolic transverse static displacement field and the need for an appropriate initial guess for the transverse displacement field in cases where initial corrugations or wrinkles are present. The insights gained from this study can aid in achieving better performance and reliability in 2D drum fabrication and contribute to accurate and robust mechanical characterization of ultra-thin materials.

## Methods

### Fabrication method

The fabrication procedure of the devices is illustrated in Fig. 4a–c. As Fig. 4a shows, we first prepare a Si (100) target substrate containing holes made using deep reactive ion etching with diameters ranging from 60 to 1000  $\mu$ m. Next, we deposit multi-layer graphene using chemical vapor deposition (CVD) on a thin-film Mo catalyst, as shown in Fig. 4b. The final stage of the fabrication procedure is the transfer of CVD-grown graphene from the growth substrate to the target substrate using a wet transfer process, as depicted in Fig. 4c.

The fabrication process resulted in the production of a set of 16 unique devices, denoted as D1–D16, which were spread among different chips. For a comprehensive description of the fabrication method, please refer to Supplementary Note 10. The drums had a range of radii ( $R$ ) from 61 to 1032  $\mu$ m. We measured the thickness ( $h$ ) of the CVD graphene on all chips using atomic force microscopy (AFM) and found that  $h$  ranges from 7 to 13.8 nm (see Supplementary Note 11).

### Measurement methodology

To probe the nanomechanical vibrations of the devices, we use a piezo shaker to drive the drums into resonance and a Polytec MSA400 laser Doppler vibrometry (LDV) system to measure their velocity in the out-of-plane direction (see Fig. 4d). The LDV actuates the piezo shaker at a specific

frequency  $f$  while simultaneously recording the position-dependent displacement  $z_f$  of the device using a 632 nm He–Ne laser with a spot diameter of  $\sim 5$   $\mu$ m. All measurements are conducted at room temperature inside a vacuum chamber at  $10^{-4}$  mbar. It should be noted that even though measurements are performed at room temperature, local heating from the laser can alter membrane properties and stress fields, especially in the nonlinear regime. To circumvent this problem, we performed our measurements at very low laser powers and ensured that the motion was probed in the linear regime of operation (see refs. 50,51). Figure 4e displays the measured first four resonances of device D1.

### Data availability

The data that support the findings of this study are available from the corresponding author upon reasonable request.

### Code availability

The data that support the findings of this study are available on reasonable request from the corresponding authors.

Received: 8 November 2023; Accepted: 4 July 2024;

Published online: 15 July 2024

## References

1. Lemme, M. C. et al. Nanoelectromechanical sensors based on suspended 2D materials. *Research* **2020**, 8748602 (2020).
2. Yildirim, T. et al. Towards future physics and applications via two-dimensional material NEMS resonators. *Nanoscale* **12**, 22366–22385 (2020).
3. Hu, K. M. et al. Resonant nano-electromechanical systems from 2D materials. *EPL* **131**, 58001 (2020).
4. Todorovic, D. et al. Multilayer graphene condenser microphone. *2D Mater.* **2**, 045013 (2015).
5. Šiškins, M. et al. Magnetic and electronic phase transitions probed by nanomechanical resonators. *Nat. Commun.* **11**, 2698 (2020).
6. Dolleman, R. J. et al. Optomechanics for thermal characterization of suspended graphene. *Phys. Rev. B* **96**, 165421 (2017).
7. Liu, H. et al. Tuning heat transport in graphene by tension. *Phys. Rev. B* **108**, L081401 (2023).
8. Roslon, I. E. et al. Probing nanomotion of single bacteria with graphene drums. *Nat. Nanotechnol.* **17**, 637–642 (2022).
9. Ferrari, P. F., Kim, S. & van der Zande, A. M. Nanoelectromechanical systems from two-dimensional materials. *Appl. Phys. Rev.* **10**, 030802 (2023).
10. Akinwande, D. et al. A review on mechanics and mechanical properties of 2D materials-Graphene and beyond. *Extrem. Mech. Lett.* **13**, 42–77 (2017).
11. Vozmediano, M. A., Katsnelson, M. I. & Guinea, F. 2010 Gauge fields in graphene. *Phys. Rep.* **496**, 109–148 (2010).
12. Chen, W. Rinkling of two-dimensional materials: Methods, properties and applications. *Nanoscale Horiz.* **4**, 291–320 (2019).
13. Deng, S. & Berry, V. 2016. Wrinkled, rippled and crumpled graphene: an overview of formation mechanism, electronic properties, and applications. *Mater. Today* **19**, 197–212 (2016).
14. Steeneken, P. G., Dolleman, R. J., Davidovikj, D., Alijani, F. & Van der Zant, H. S. Dynamics of 2D material membranes. *2D Mater.* **8**, 042001 (2021).
15. Gornyi, I. V., Kachorovskii, V. Y. & Mirlin, A. D. 2016 Anomalous Hooke's law in disordered graphene. *2D Mater.* **4**, 011003 (2016).
16. Sarafraz, A. et al. Nonlinear elasticity of wrinkled atomically thin membranes. *J. Appl. Phys.* **130**, 184302 (2021).
17. Paillet, M., Parret, R., Sauvajol, J. L. & Colombari, P. Graphene and related 2D materials: an overview of the Raman studies. *J. Raman Spectrosc.* **49**, 8–12 (2018).
18. Dai, Z., Liu, L. & Zhang, Z. Strain engineering of 2D materials: issues and opportunities at the interface. *Adv. Mater.* **31**, 1805417 (2019).

19. Colangelo, F. et al. Mapping the mechanical properties of a graphene drum at the nanoscale. *2D Mater.* **6**, 025005 (2019).
20. Ferralis, N. Probing mechanical properties of graphene with Raman spectroscopy. *J. Mater. Sci.* **45**, 5135–5149 (2010).
21. Eichler, A. et al. Nonlinear damping in mechanical resonators made from carbon nanotubes and graphene. *Nat. Nanotechnol.* **6**, 339–342 (2011).
22. Bunch, J. S. et al. Impermeable atomic membranes from graphene sheets. *Nano Lett.* **8**, 2458–2462 (2008).
23. Morell, N. et al. High quality factor mechanical resonators based on WSe<sub>2</sub> monolayers. *Nano Lett.* **16**, 5102–5108 (2016).
24. Houri, S. et al. Direct and parametric synchronization of a graphene self-oscillator. *Appl. Phys. Lett.* **110**, 073103 (2017).
25. Van Leeuwen, R. et al. Time-domain response of atomically thin MoS<sub>2</sub> nanomechanical resonators. *Appl. Phys. Lett.* **105**, 043102 (2014).
26. Steeneken, P. G. et al. Dynamics of 2D material membranes. *2D Mater.* **8**, 042001 (2021).
27. Reddy, J. N. *Theory and Analysis of Elastic Plates and Shells*. (CRC Press, 2006).
28. Amabili, M. *Nonlinear Vibrations and Stability of Shells and Plates*. (Cambridge University Press, 2008).
29. Keşkekler, A. et al. Tuning nonlinear damping in graphene nanoresonators by parametric-direct internal resonance. *Nat. Commun.* **12**, 1099 (2021).
30. Waitz, R. et al. Spatially resolved measurement of the stress tensor in thin membranes using bending waves. *Phys. Rev. Appl.* **3**, 044002 (2015).
31. Davidovikj, D. et al. Nonlinear dynamic characterization of two-dimensional materials. *Nat. Commun.* **8**, 1253 (2017).
32. Sajadi, B. et al. Size-and temperature-dependent bending rigidity of graphene using modal analysis. *Carbon* **139**, 334–341 (2018).
33. Sajadi, B. et al. Nonlinear dynamic identification of graphene's elastic modulus via reduced order modeling of atomistic simulations. *J. Mech. Phys. Solids* **122**, 161–176 (2019).
34. Davidovikj, D. et al. Visualizing the motion of graphene nanodrums. *Nano Lett.* **16**, 2768–2773 (2016).
35. Castellini, P., Martarelli, M. & Tomasini, E. P. Laser Doppler vibrometry: development of advanced solutions answering to technology's needs. *Mech. Syst. Signal. Process.* **20**, 1265–1285 (2006).
36. Castellanos-Gomez, A. et al. Single-layer MoS<sub>2</sub> mechanical resonators. *Adv. Mater.* **25**, 6719–6723 (2013).
37. Chen, C. et al. Performance of monolayer graphene nanomechanical resonators with electrical readout. *Nat. Nanotechnol.* **4**, 861–867 (2009).
38. Van der Zande, A. M. et al. Large-scale arrays of single-layer graphene resonators. *Nano Lett.* **10**, 4869–4873 (2010).
39. Mohiuddin, T. M. G. et al. Uniaxial strain in graphene by Raman spectroscopy: G peak splitting, Grüneisen parameters, and sample orientation. *Phys. Rev. B* **79**, 205433 (2009).
40. Katsnelson, M. I. & Fasolino, A. Graphene as a prototype crystalline membrane. *Acc. Chem. Res.* **46**, 97–105 (2013).
41. Sarafraz, A. et al. Pressure-induced nonlinear resonance frequency changes for extracting Young's modulus of nanodrums. *Nonlinear Dyn.* **111**, 14751–14761 (2023).
42. Sajadi, B. et al. Experimental characterization of graphene by electrostatic resonance frequency tuning. *J. Appl. Phys.* **122**, 234302 (2017).
43. Li, S. R., Yu, W. S. & Batra, R. C. Free vibration of thermally pre/post-buckled circular thin plates embedded with shape memory alloy fibers. *J. Therm. Stresses* **33**, 79–96 (2010).
44. Changguo, W., Yunliang, L., Xingwen, D., Xiaodong, H. & Guozhi, S. Simulation analysis of vibration characteristics of wrinkled membrane space structure. *Int. J. Space Struct.* **22**, 239–246 (2007).
45. Neumann, C. et al. Raman spectroscopy as probe of nanometre-scale strain variations in graphene. *Nat. Commun.* **6**, 8429 (2015).
46. Hiltunen, V. M. et al. Ultrastiff graphene. *npj 2D Mater. Appl.* **5**, 49 (2021).
47. Liu, H. et al. Enhanced sensitivity and tunability of thermomechanical resonance near the buckling bifurcation. *2D Mater.* **11**, 025028 (2024).
48. Kukathasan, S. & Pellegrino, S., 2003. Nonlinear vibration of wrinkled membranes. 44th AIAA/ASME/ASCE/AHS/ASC Structures, Structural Dynamics, and Materials Conference, p. 1747.
49. Šiškins, M. et al. 2019. Highly anisotropic mechanical and optical properties of 2D layered As<sub>2</sub>S<sub>3</sub> membranes. *ACS Nano* **13**, 10845–10851.
50. Liu, H., Lee, M., Šiškins, M., Van Der Zant, H. S., Steeneken, P. G. & Verbiest, G. J. Tuning heat transport in graphene by tension. *Phys. Rev. B* **108**, L081401 (2023).
51. Liu, H. et al. Optomechanical methodology for characterizing the thermal properties of 2D materials. *APL Mater.* **12**, 020901 (2024).

## Acknowledgements

This project has received funding from the European Union's Horizon 2020 research and innovation program under Grant Agreement Nos. 802093 (ERC starting grant ENIGMA), 785219, and 881603 (Graphene Flagship). Katarina Cvetačović and Marko Spasenović acknowledge support from the Serbian Ministry of Science, Technological Development, and Innovations, contract number 451-03-47/2023-01/200026. Farbod Aljani further acknowledges financial support from the European Union Framework Program for Research and Innovation, Horizon Europe, under ERC Consolidator grant NCANTO (101125458).

## Author contributions

K.C., M.S., and S.V. prepared the samples. H.L. and T.M.G. performed the experiments. A.S. developed the theory and performed the simulations. G.V., F.A., M.S., and P.G.S. designed and supervised the project. The manuscript was written by A.S., H.L., G.V., and F.A., with all authors agreeing on its content.

## Competing interests

The authors declare no competing interests.

## Additional information

**Supplementary information** The online version contains supplementary material available at <https://doi.org/10.1038/s41699-024-00485-6>.

**Correspondence** and requests for materials should be addressed to Ali Sarafraz or Gerard J. Verbiest.

**Reprints and permissions information** is available at <http://www.nature.com/reprints>

**Publisher's note** Springer Nature remains neutral with regard to jurisdictional claims in published maps and institutional affiliations.

**Open Access** This article is licensed under a Creative Commons Attribution 4.0 International License, which permits use, sharing, adaptation, distribution and reproduction in any medium or format, as long as you give appropriate credit to the original author(s) and the source, provide a link to the Creative Commons licence, and indicate if changes were made. The images or other third party material in this article are included in the article's Creative Commons licence, unless indicated otherwise in a credit line to the material. If material is not included in the article's Creative Commons licence and your intended use is not permitted by statutory regulation or exceeds the permitted use, you will need to obtain permission directly from the copyright holder. To view a copy of this licence, visit <http://creativecommons.org/licenses/by/4.0/>.

© The Author(s) 2024